Engineering Transactions, **72**(3): 343–363, 2024, doi: 10.24423/EngTrans.3230.2024
Institute of Fundamental Technological Research Polish Academy of Sciences (IPPT PAN)
Université de Lorraine • Poznan University of Technology

Research Paper

Unbalanced Response Analysis and Experiment of Magnetic Levitation Rotor Based on the State-Space Method

Shuyue ZHANG[1)*], Yahu ZHANG[1)], Xiaolian LV[1)], Songling JIN[2)]

[1)] *School of Mechanical and Electrical Engineering, Chuzhou University*
Chuzhou 239000, China

[2)] *Anhui Ming Hui Electric Company Limited*
Chuzhou 239000, China

*Corresponding Author e-mail: zhangshuyue@chzu.edu.cn

Magnetic levitation compressors are critical for producing large flow rates of superfluid helium. The steady operation of these compressors depends heavily on the unbalanced response characteristic of their rotors. Previous research, utilizing traditional unbalance response calculation methods, primarily focused on displacement response while neglecting current response. This paper transforms the finite element model of the magnetic levitation rotor into a state-space representation. It then investigates the influence of vital parameters on both displacement and current responses. The results of speed-up experiment carried out on the compressor prototype test rig agree with the simulation results. The study indicates that adjusting control parameters can suppress vibration and simultaneously reduce control current. This work is essential for the application of compressors in the superfluid helium system.

Keywords: electromagnetic bearing; displacement response; current response; state-space method.

Notations

A – magnetic pole area,
$\mathbf{A}$ – state matrix,
$\mathbf{B}$ – input matrix,
$\mathbf{C}$ – output matrix,
$\mathbf{D}$ – feedthrough matrix or damping matrix,
e – eccentricity of the unbalance mass,
$\mathbf{e}$ – displacement deviation signal,
f – cut-off frequency,
$\mathbf{f}$ – force,
$\mathbf{F}$ – generalized force extended by conversion matrix,

$\mathbf{G}$ – gyro matrix of the rotor model,
i – bias current,
K – gain,
K_p – proportional gain,
K_d – derivate gain,
$\mathbf{K}$ – stiffness matrix,
m – unbalanced masses,
$\mathbf{M}$ – mass matrix,
N – coil turns of magnetic bearing,
$\mathbf{q}$ – displacement vector,
T – time constant,
$\mathbf{T}$ – conversion matrix,
$\mathbf{T}_{re}$ – regular modal matrix applying to decouple and normalize the FEM model,
x_0 – bias displacement,
$\mathbf{x}$ – state vector,
$\mathbf{y}$ – output vector.

Greek characters

μ_0 – vacuum permeability,
ξ_a – attenuation constant,
φ – phase angle of the unbalanced mass,
ω – rotor rotation speed, or corner frequency.

Subscripts

a – amplifier,
amb – active magnetic bearing,
c – controller,
cl – closed loop system,
d – differential term,
i – integration term, or control current,
ol – open loop system,
p – proportional term,
r – rotor model, or reference input,
re – simplified system matrixes,
rf – input matrix corresponding to disturbance force,
ri – input matrix corresponding to control current,
s – sensor,
u – unbalanced mass force.

1. Introduction

Super-fluid helium has increasingly been applied in fields such as high-energy physics, nuclear fusion, and superconductivity. The only way to obtain 2K super-fluid helium on a large scale nowadays is by using multistage centrifugal cold compressors to reduce the pressure and temperature of the sub-cooling tank [1]. Due to the unique operating conditions of cold compressors, traditional grease-

lubricated bearings and gas bearings struggle to meet the support requirements. Active magnetic bearings (AMBs) levitate the rotor using control current, making them highly suitable for extreme conditions such as clean environments, vacuum, and super-high speeds [2]. AMBs are currently the optimal support devices for cold compressor rotors in superfluid helium systems [3].

The compressor's smooth operation is crucial for the successful commissioning of the superfluid helium system. Researchers have developed various control methods to realize the rotors' stable suspension and rotation [4–6]. However, proportional integral derivative (PID) control remains the simplest and most effective method [7–9]. Simply applying a PID controller can ensure the smooth rotation of a rigid rotor [10].

The unbalanced vibration of the rotor, as the primary vibration source during operation, has been one a major challenge [10–14]. Wang *et al.* [10] and Gao *et al.* [15] simplified the AMB-rotor system to a single-degree-of-freedom model and employed an analytical solution method to study displacement vibration at different rotation frequencies. Other researchers have developed lower-order models, such as discrete mass models based on the transfer matrix or four-degree-of-freedom rigid body models. Then, they applied standard methods such as the fourth-order Runge-Kutta method [11], Newmark-β [12], and Wilson-θ [12], among others, to obtain the time-domain solution. Finally, they used the Fourier transform to analyze the frequency domain response. Tang *et al.* [13] and Lei and Palazzolo [17] constructed finite element models and applied modal superposition method to determine the transient response. These approaches directly reference and apply traditional methods for analyzing unbalanced vibration in rotors, offering precise physical interpretations and facilitating understanding. However, there are some problems with these methods. To transform the function of electronic control hardware into resultant stiffness and damping, it is often necessary to simplify the effects of power amplifiers and sensors to constant gains and to replace the controllers with the simplest PD/PID form [10, 11, 16, 18]. These assumptions may deviate from actual conditions and result in inaccurate modeling and simulation results. Additionally, these PID parameters obtained through simulation might not be directly usable, and significant effort is still needed to tune the parameters experimentally. Furthermore, the so-called 'equivalence' poses challenges for calculating the control signal because these analysis methods often ignore the coil current calculation during rotor operation. Conversely, coil current is a significant physical quantity. Low coil current can lead to poor anti-interference ability. Pursuing a high-rigidity system to reduce vibration amplitude, at the cost of high coil current, may cause the power amplifier and coil magnetic field to saturate.

With the help of modern control theory [19, 20], this paper establishes a complete state-space model of the closed-loop system for the magnetic levitation

rotor controlled by PID. The frequency response equations are derived by considering the unbalanced force as the system input and g the rotor displacement and control current as system outputs. The influence of key control parameters on the unbalanced response is analyzed. Finally, the unbalanced response is experimentally verified on the prototype test rig for compressors. The excellent agreement between experiment and simulation results demonstrates the validity of the modeling and dynamic characteristics analysis methods. This work is of great significance for the actual commissioning of magnetic levitation compressor in the superfluid helium refrigeration systems.

2. Modeling for Magnetic levitation rotor system

Figure 1 shows the cold compressor model for the third stage in the superfluid helium refrigeration system. Close to the two radial AMBs are two inductive displacement sensors. The permanent magnet synchronous motor is centrally located.

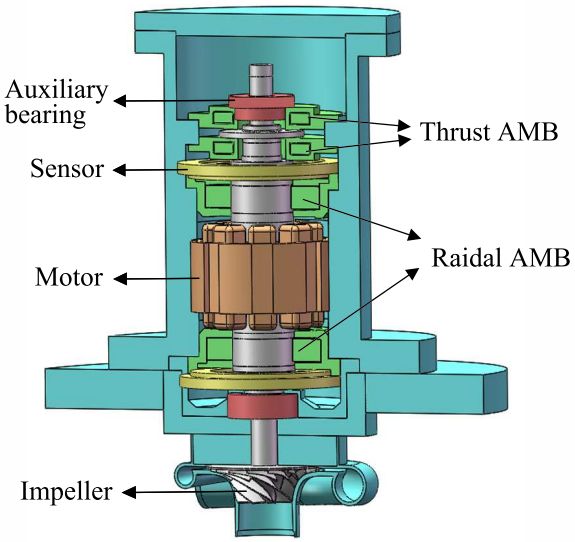

Fig. 1. Sectional structure of magnetic levitation cold compressor.

To systematically develop an appropriate analysis model, we divide the system into two parts: the AMB-rotor system and the electronic control system. The remainder of this section is devoted to discussing the modeling of each component.

2.1. AMB-rotor system modeling

Figure 2 presents a photograph of the magnetic levitation rotor for cold compressor. The rotor assembly consists of an internal shaft core, thrust plate, shaft sleeve, impeller, and other components. The shaft, fabricated from 40Cr steel, has a diameter of approximately 38 mm. The shaft sleeve includes the silicon steel laminate of the radial AMB, sensors, and a centrally located motor sleeve. Both ends of the sleeve are designed with a circular pattern of threaded holes to detect and counteract unbalanced mass. The motor sleeve, made from samarium cobalt permanent magnet material, and exhibits an elastic modulus half that of the shaft.

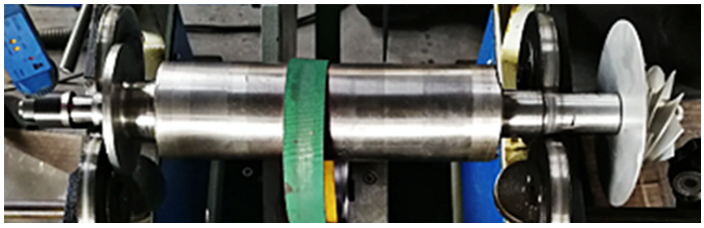

FIG. 2. Photograph of the magnetic levitation rotor for cold compressor.

Figure 3 presents the finite element model (FEM) of the magnetic levitation rotor. We build the rotor model based on Timoshenko beam theory. The shaft, depicted in cyan color, and the motor sleeve, in green are all integrated and considered as flexible shaft units. The thrust plate, AMB silicon steel sheets, sensors, impeller, and compression nuts have little impact on the rotor's lateral bending. Therefore, they are modeled as rigid discs, colored blue.

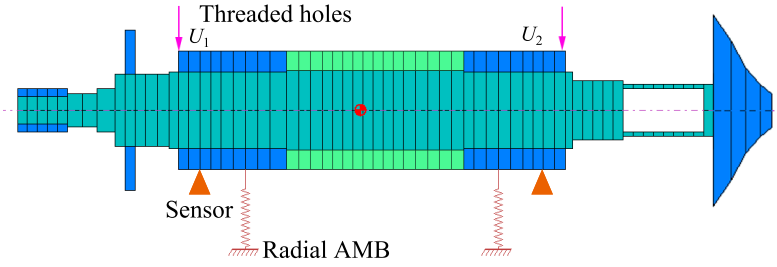

FIG. 3. FEM of the magnetic levitation rotor.

When dividing nodes, key positions such as AMBs, sensors, and threaded holes are designated as primary nodes. The sub-nodes are distributed between primary nodes to ensure uniform spacing and computational convergence. Finally, the rotor model with 64 nodes is obtained. Each node is equipped with two translational and two rotational degrees of freedom (DOF).

The rotor dynamic equation with MATLAB could be assembled as follows:

$$\mathbf{M}_r\ddot{\mathbf{q}}_r + \underbrace{(\mathbf{C}_r + \omega\mathbf{G}_r)}_{\mathbf{D}_r}\dot{\mathbf{q}}_r + \mathbf{K}_r\mathbf{q}_r = \mathbf{F}_u + \mathbf{F}_a, \tag{2.1}$$

where $\mathbf{q}_r$ is the rotor displacement vector, $\mathbf{M}_r$, $\mathbf{C}_r$, $\mathbf{G}_r$, and $\mathbf{K}_r$ are the rotor's mass matrix, damping, gyroscopic, and stiffness matrices, respectively, ω is the rotor rotational speed, and $\mathbf{F}_u$ and $\mathbf{F}_a$ are the unbalanced force and active electromagnetic forces, modeled below.

The unbalance at points U_1 and U_2 in Fig. 3 is 1.06 g · mm and 0.82 g · mm, respectively, and their phase angle is 171°. The unbalanced force $\mathbf{f}_u$ due to mass eccentricity can be expressed as:

$$\mathbf{f}_u(t) = \omega^2 \begin{bmatrix} m_{e1}e_1(\cos\varphi_1 + \sin\varphi_1) \\ m_{e1}e_1(\sin\varphi_1 - \cos\varphi_1) \\ m_{e2}e_2(\cos\varphi_2 + \sin\varphi_2) \\ m_{e2}e_2(\sin\varphi_2 - \cos\varphi_2) \end{bmatrix} \mathrm{e}^{-\mathrm{j}\omega t}, \tag{2.2}$$

where m_e, e, and φ represent the unbalanced masses, eccentricities and phase angles, respectively, t is time, and j is the imaginary unit.

By introducing the conversion matrix $\mathbf{T}_u$, related to the nodes where threaded holes are located, the unbalanced force $\mathbf{f}_u$ is extended to the generalized unbalanced force $\mathbf{F}_u$:

$$\mathbf{F}_u = \mathbf{T}_u\mathbf{f}_u. \tag{2.3}$$

We use radial magnetic bearings with an eight-pole structure. The main parameters are as follows: the magnetic pole area is $A = 246$ mm^2, the number of winding turns is $N = 93$, and the air gaps of the protective bearing and the radial magnetic bearing are 0.15 mm and 0.35 mm, respectively.

Thus, the four DOF electromagnetic forces provided by the two radial AMBs are usually expressed with a linear model [2]:

$$\mathbf{f}_a = \left[4\cos\left(\frac{\pi}{8}\right)\mu_0 N^2 A\right]\frac{i_0}{x_0^2}\mathbf{i}_a + \left[4\cos\left(\frac{\pi}{8}\right)\mu_0 N^2 A\right]\frac{i_0^2}{x_0^3}\mathbf{q}_r = k\frac{i_0}{x_0^2}\mathbf{i}_a + k\frac{i_0^2}{x_0^3}\mathbf{q}_r, \tag{2.4}$$

where μ_0 is the vacuum permeability, $\mathbf{i}_a$ is the control current, and x_0 and i_0 are the bias displacement and bias current, respectively. Generally, the bias displacement is the stator center. The bias current is limited by the bandwidth of the power amplifier and the saturation of the magnetic field.

With the electromagnetic force conversion matrix $\mathbf{T}_a$, the unbalanced force $\mathbf{f}_a$ can be extended to the generalized unbalanced force $\mathbf{F}_a$:

$$\mathbf{F}_a = \mathbf{T}_a \mathbf{f}_a = \mathbf{T}_a k \frac{i_0}{x_0^2} \mathbf{i}_a + \mathbf{T}_a k \frac{i_0^2}{x_0^3} \mathbf{T}_a^{\mathrm{T}} \mathbf{q}_r. \tag{2.5}$$

Substituting Eqs. (2.3) and (2.5) into Eq. (2.1) gives:

$$\mathbf{M}_r \ddot{\mathbf{q}}_r + \mathbf{D}_r \dot{\mathbf{q}}_r + \left(\mathbf{K}_r + \mathbf{T}_a k \frac{i_0^2}{x_0^3} \mathbf{T}_a^{\mathrm{T}} \right) \mathbf{q}_r = \mathbf{T}_a k \frac{i_0}{x_0^2} \mathbf{i}_a + \mathbf{T}_u \mathbf{f}_u. \tag{2.6}$$

2.2. State-space realization of the rotor model

Even without considering the electronic control system, the rotor model in Eq. (2.6) has 256 states. Such a large model is unwieldy for controller design and unbalanced response analysis. As low-frequency modes dominate the rotor vibration, we apply the modal truncation method to describe the dynamic behavior [21]. The degree of model reduction should be adapted to the compressor's working speed and the rotor's natural frequency.

Figure 4 shows the Campbell diagram of the open-loop system. The first two-order rigid modes of the rotor mainly depend on the controller, which will be discussed later. The first and second bending critical speeds indicated by the simulation results are 2500 Hz and 4820 Hz, respectively. We conducted rotor model tests with a force hammer to verify these frequencies. The results shown in Fig. 5 demonstrate consistency between the experimental results and the simulation results. The compressor's rated speed is 833 Hz, significantly lower

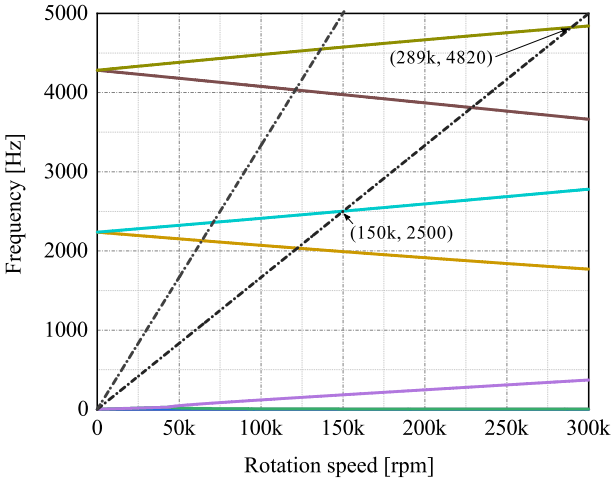

FIG. 4. Campbell diagram.

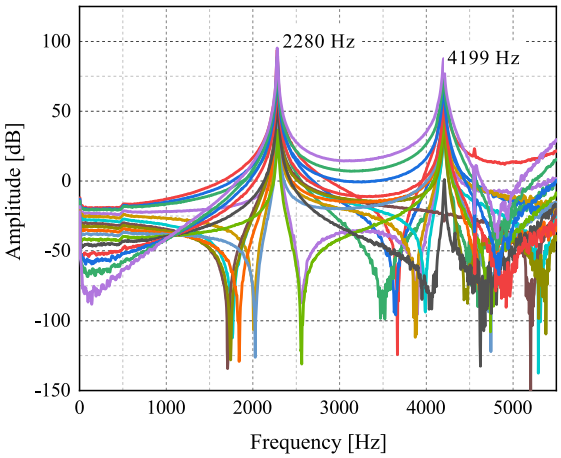

FIG. 5. Modal test results.

than the first bending critical speed. Ultimately, we retained the first three-order modes of the rotor model in their entirety.

A regular modal matrix, truncated by the cut-off eigenforms, is applied to decouple and normalize the rotor's FEM. The simplified system matrixes are marked with the subscript

$$\mathbf{M}_{re} = \mathbf{T}_{re}^{\mathrm{T}}\mathbf{M}_r\mathbf{T}_{re}, \qquad \mathbf{D}_{re} = \mathbf{T}_{re}^{\mathrm{T}}\mathbf{D}_r\mathbf{T}_{re}, \quad \mathbf{I}_{re} = \mathbf{T}_{re}^{\mathrm{T}}\mathbf{T}_a k\frac{i_0}{x_0^2},$$

$$\mathbf{K}_{re} = \mathbf{T}_{re}^{\mathrm{T}}\left(\mathbf{K}_r + \mathbf{T}_a k\frac{i_0^2}{x_0^3}\mathbf{T}_a^{\mathrm{T}}\right)\mathbf{T}_{re}, \quad \mathbf{F}_{re} = \mathbf{T}_{re}^{\mathrm{T}}\mathbf{T}_u, \qquad \mathbf{q}_{re} = \mathbf{T}_{re}\,\mathbf{q}_r.$$

The equations in Eq. (2.6) are decoupled and reduced as follows:

$$\mathbf{M}_{re}\,\ddot{\mathbf{q}}_{re} + \mathbf{D}_{re}\dot{\mathbf{q}}_{re} + \mathbf{K}_{re}\mathbf{q}_{re} = \mathbf{I}_{re}\,\mathbf{i}_a + \mathbf{F}_{re}\,\mathbf{f}_u. \tag{2.7}$$

If we define the state vector $\mathbf{x}_r = \begin{bmatrix}\dot{\mathbf{q}}_{re} & \mathbf{q}_{re}\end{bmatrix}^{\mathrm{T}}$, then we can transform Eq. (2.7) into a state-space form:

$$\begin{cases} \dot{\mathbf{x}}_r = \underbrace{\begin{bmatrix}\mathbf{0} & \mathbf{I} \\ -\mathbf{M}_{re}^{-1}\mathbf{K}_{re} & -\mathbf{M}_{re}^{-1}\mathbf{D}_{re}\end{bmatrix}}_{\mathbf{A}_r}\mathbf{x}_r + \underbrace{\begin{bmatrix}\mathbf{0} \\ \mathbf{M}_{re}^{-1}\mathbf{I}_{re}\end{bmatrix}}_{\mathbf{B}_{ri}}\mathbf{i}_a + \underbrace{\begin{bmatrix}\mathbf{0} \\ \mathbf{M}_{re}^{-1}\mathbf{F}_{re}\end{bmatrix}}_{\mathbf{B}_{rf}}\mathbf{f}_u, \\ \mathbf{y}_r = \mathbf{C}_r\mathbf{x}_r. \end{cases} \tag{2.8}$$

The vector $\mathbf{y}_r$ represents the rotor displacement at sensor locations specified by the coefficient distribution matrix $\mathbf{C}_r$.

2.3. Electronic control hardware model

Figure 6 presents the block diagram of the closed-loop control system. The simulation results depend on model accuracy. Previous research often oversimplifies the electronic control hardware, representing its impact on stiffness and damping as constant gains. Moreover, completed PID controllers are frequently reduced to PD controllers [10, 11, 14]. However, there is a discrepancy between the simulation model and the actual situation. To address this, the section establishes more detailed and accurate models for the controller, power amplifier, and sensor.

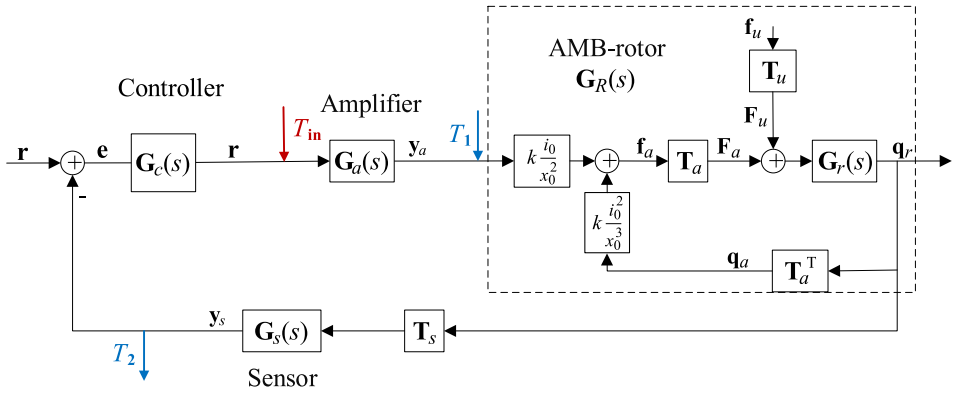

FIG. 6. Closed-loop feedback block diagram of the AMB-rotor system.

Power amplifier characteristics are affected by coil inductance, resistance, and eddy current [22]. However, the effects of the eddy current are usually small and can be ignored when modeling. We use Agilent Dynamic Signal Analyzer 35670A to perform a sine sweep, and then the amplitude-frequency characteristics of the amplifier are experimentally measured, as shown in Fig. 7. The transfer function of the amplifier model, fitted to the experimental frequency response, is:

$$G_a(s) = \frac{K_a\omega_a^2}{s^2 + 2\xi_a\omega_a s + \omega_a^2} \frac{s^2 - \frac{6}{T_a}s + \frac{12}{T_a^2}}{s^2 + \frac{6}{T_a}s + \frac{12}{T_a^2}}. \tag{2.9}$$

The corner frequency ω_a is 2300 Hz, the attenuation constant ξ_a is 1.2, the gain K_a is 0.79 A/V. A second-order Padé approximation is modeled for the time delay due to digital-analog conversion and PWM modulation. The time constant τ_a is set to 100 μs.

The compressor rotor is rigid, so the PID control method can meet engineering requirements. To avoid the displacement deviation signal's infinite amplifi-

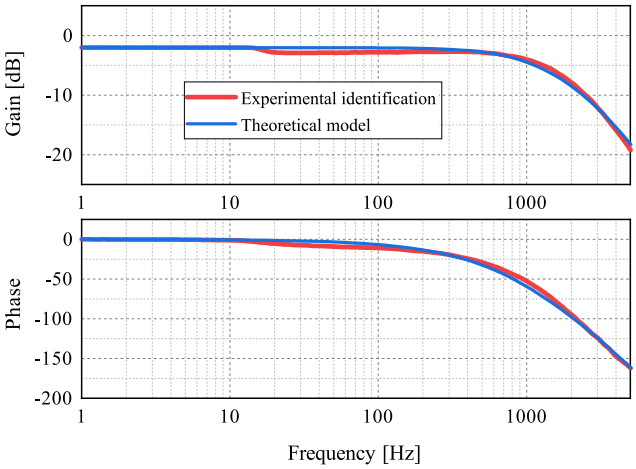

FIG. 7. Frequency characteristic of the power amplifier.

cation at low and high frequencies, we apply a PID controller with incomplete derivative and incomplete integral, as shown below:

$$G_c(s) = K_p + \frac{K_i}{\frac{1}{2\pi f_i}s + 1} + \frac{K_d s}{\frac{1}{2\pi f_d}s + 1}, \tag{2.10}$$

where f_d is the cut-off frequency of the differential term, related to the operation frequency, and is set at 600 Hz, and f_i is the cut-off frequency of the integration, set at 0.75 Hz.

The two most important parameters for the PID controller are the proportional gain K_p and the derivative gain K_d. They determine the stability and dynamic performance of the rotor. Many studies [2, 10] have examined the relationship between proportional gain and the resultant stiffness. We assume the resultant stiffness to be 1 to 3 times the displacement stiffness of the AMB and take the damping ratio of the closed-loop system to be 20% to 70%. Therefore, we estimate the ranges of proportional gain and differential gain as: $K_p \in (0.27,\ 0.80)$, $K_d \in (3 \cdot 10^{-4},\ 11 \cdot 10^{-4})$.

Differential transformer-type inductance sensors are used to measure rotor displacement. Low-pass filters are designed to suppress aliasing effects during digitization. Within the linear range, the first-order mathematical description of the sensor combing with the low-pass filter is:

$$G_s(s) = \frac{K_s}{T_s s + 1}, \tag{2.11}$$

where the magnification K_s is 20 kV/m, and the time constant T_s is $5 \cdot 10^{-5}$.

The following state-space equations describe the models of the amplifiers, controllers, and sensors. To distinguish these models, the subscripts a, c, and s will be used accordingly.

$$\begin{cases} \dot{\mathbf{x}} = \mathbf{A}\mathbf{x} + \mathbf{B}\mathbf{u}, \\ \mathbf{y} = \mathbf{C}\mathbf{x} + \mathbf{D}\mathbf{u}. \end{cases} \tag{2.12}$$

In the above equation, the feedthrough matrices of both the amplifiers and sensors are zero.

3. State-space realization

The conventional method of solving the unbalanced response involves replacing the current signal in Eq. (2.8) with the displacement, based on their mathematical relationship. Using this approach, the time-domain solution for displacement can be obtained by applying standard methods for solving partial differential equations [10–13, 15, 16]. However, since the partial differential equation does not include control signals, this approach complicates solving for the control signal. This paper establishes a state-space model that includes all components of the closed-loop system. The variables of interest are extracted as inputs and outputs, and then the unbalanced response is obtained by solving the corresponding transfer functions.

3.1. Open-loop system

It is convenient to first calculate the open-loop system model, which will later help in deriving the closed-loop system model. Figure 8 is the open-loop system,

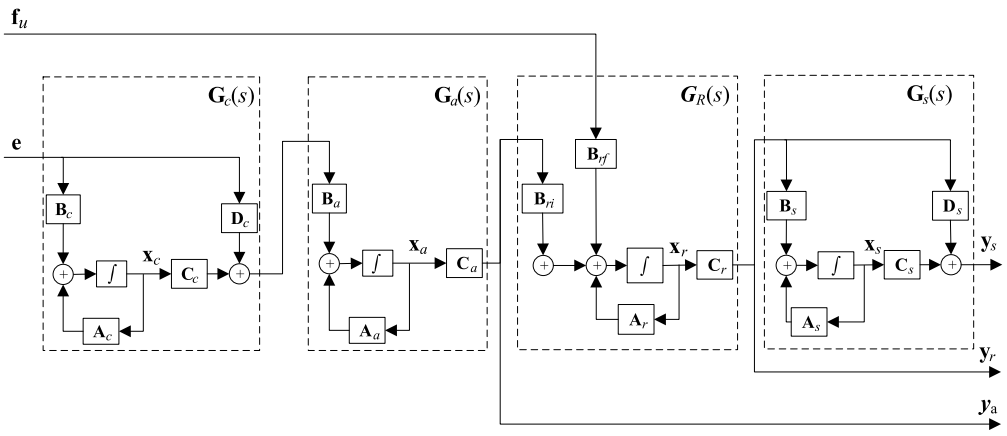

Fig. 8. Open-loop system model.

combing the controller, amplifier model, and sensor model with the AMB-rotor state-space model. The output vectors include the sensor measurement signal $\mathbf{y}_s$, rotor displacement $\mathbf{y}_r$, and control signal $\mathbf{y}_a$. The state vectors include unbalanced forces $\mathbf{f}_u$ and the controller input signal $\mathbf{e}$. Thus, the state-space equation of the open-loop system is derived as follows:

$$
\begin{cases}
\begin{bmatrix} \dot{\mathbf{x}}_s \\ \dot{\mathbf{x}}_r \\ \dot{\mathbf{x}}_a \\ \dot{\mathbf{x}}_c \end{bmatrix} = \begin{bmatrix} \mathbf{A}_s & \mathbf{B}_s\mathbf{C}_r & \mathbf{0} & \mathbf{0} \\ \mathbf{0} & \mathbf{A}_r & \mathbf{B}_{ri}\,\mathbf{C}_a & \mathbf{0} \\ \mathbf{0} & \mathbf{0} & \mathbf{A}_a & \mathbf{B}_a\mathbf{C}_a \\ \mathbf{0} & \mathbf{0} & \mathbf{0} & \mathbf{A}_c \end{bmatrix} \begin{bmatrix} \mathbf{x}_s \\ \mathbf{x}_r \\ \mathbf{x}_a \\ \mathbf{x}_c \end{bmatrix} + \begin{bmatrix} \mathbf{0} & \mathbf{0} \\ \mathbf{B}_{rf} & \mathbf{0} \\ \mathbf{0} & \mathbf{B}_a\mathbf{D}_c \\ \mathbf{0} & \mathbf{B}_c \end{bmatrix} \begin{bmatrix} \mathbf{f}_u \\ \mathbf{e} \end{bmatrix}, \\
\begin{bmatrix} \mathbf{y}_s \\ \mathbf{y}_r \\ \mathbf{y}_a \end{bmatrix} = \begin{bmatrix} \mathbf{C}_s & \mathbf{D}_s\mathbf{B}_c\mathbf{C}_r & \mathbf{0} & \mathbf{0} \\ \mathbf{0} & \mathbf{C}_r & \mathbf{0} & \mathbf{0} \\ \mathbf{0} & \mathbf{0} & \mathbf{C}_a & \mathbf{0} \end{bmatrix} \begin{bmatrix} \mathbf{x}_s \\ \mathbf{x}_r \\ \mathbf{x}_a \\ \mathbf{x}_c \end{bmatrix}.
\end{cases} \tag{3.1}
$$

3.2. Closed-loop system

Figure 9 shows the feedback control block diagram. The displacement deviation signal $\mathbf{e}$ is given by:

$$
\mathbf{e} = \mathbf{r} - \mathbf{y}_s. \tag{3.2}
$$

By substituting Eq. (3.1) into (3.2), and considering the reference signal r and the unbalanced force $\mathbf{f}_u$ as new input vectors, while keeping the state variables and output variables the same as those of the open-loop system, we derived the state-space realization form of the closed-loop system as follows:

$$
\mathbf{G}_{cl} = \begin{bmatrix} \mathbf{A}_{cl} & \mathbf{B}_{clf} & \mathbf{B}_{clr} \\ & \mathbf{D}_{clsf} & \mathbf{D}_{clsr} \\ \mathbf{C}_{cl} & \mathbf{D}_{clrf} & \mathbf{D}_{clrr} \\ & \mathbf{D}_{claf} & \mathbf{D}_{clar} \end{bmatrix} \tag{3.3}
$$

$$
= \begin{bmatrix} \mathbf{A}_s & \mathbf{B}_s\mathbf{C}_r & \mathbf{0} & \mathbf{0} & \mathbf{0} & \mathbf{0} \\ \mathbf{0} & \mathbf{A}_r & \mathbf{B}_{ri}\,\mathbf{C}_a & \mathbf{0} & \mathbf{B}_{rf} & \mathbf{0} \\ -\mathbf{B}_a\mathbf{D}_c\mathbf{C}_s & -\mathbf{B}_a\mathbf{D}_c\mathbf{D}_s\mathbf{B}_s\mathbf{C}_r & \mathbf{A}_a & \mathbf{B}_a\mathbf{C}_a & \mathbf{0} & \mathbf{B}_a\mathbf{D}_c \\ -\mathbf{B}_c\mathbf{C}_s & -\mathbf{B}_c\mathbf{D}_s\mathbf{B}_s\mathbf{C}_r & \mathbf{0} & \mathbf{A}_c & \mathbf{0} & \mathbf{B}_c \\ \mathbf{C}_s & \mathbf{D}_s\mathbf{B}_c\mathbf{C}_r & \mathbf{0} & \mathbf{0} & \mathbf{0} & \mathbf{0} \\ \mathbf{0} & \mathbf{C}_r & \mathbf{0} & \mathbf{0} & \mathbf{0} & \mathbf{0} \\ \mathbf{0} & \mathbf{0} & \mathbf{C}_a & \mathbf{0} & \mathbf{0} & \mathbf{0} \end{bmatrix}.
$$

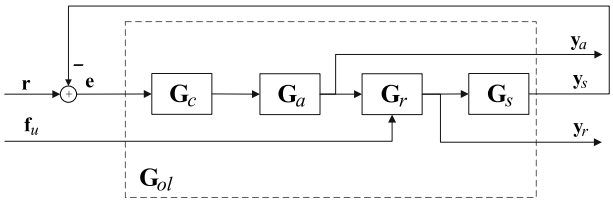

FIG. 9. Control block diagram within the closed-loop system.

3.3. Closed-loop system identification

To verify the accuracy of the closed-loop system model, a sine frequency sweep test is conducted. The sinusoidal signal is input at the amplifier's front point (marked T_{in} in Fig. 6). Then, the signal from the controlled object input terminal (labeled with T_1) to the rotor displacement output terminal (marked T_2), is analyzed. The Bode plot of the closed-loop system's first channel is shown with the red curve in Fig. 10. The blue curve represents the Bode plot of the corresponding transfer function. It is worth noting that we use the same controller parameters ($K_p = 0.35$, and $K_d = 0.00060$) for both the simulation and the experiment.

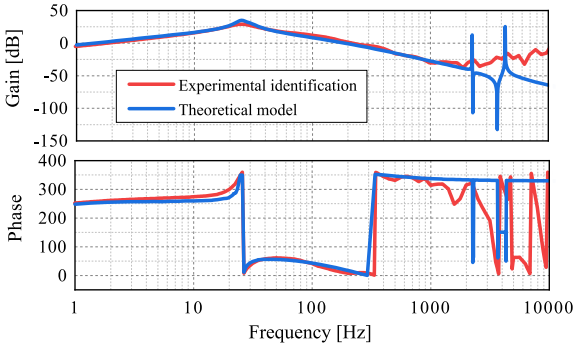

FIG. 10. Model of the magnetic levitation rotor in the closed-loop system.

The figure demonstrates that the models obtained from the simulation and experiments are relatively well-matched within 2000 Hz. The critical speeds of rigid bodies obtained by the two methods are 27 Hz and 28 Hz, respectively. However, this method cannot identify the high-frequency bending modes.

3.4. Calculation of unbalanced response

Based on the above state-space description, the transfer function from the unbalanced force to the rotor displacement signal, the sensor output signal, and the control signal can be obtained according as follows:

$$\mathbf{G}_{f\to y}(s) = \mathbf{C}_{cl}\left(\frac{\mathbf{B}_{clf}}{s\mathbf{I}-\mathbf{A}_{cl}}\right) + \begin{bmatrix}\mathbf{D}_{clrf}\\ \mathbf{D}_{clrf}\\ \mathbf{D}_{claf}\end{bmatrix}. \tag{3.4}$$

By combing Eqs. (2.3) and (3.4), the system response, including rotor displacement signals $\mathbf{y}_r$ and control current $\mathbf{y}_a$, can be calculated as follows:

$$\mathbf{y}_{fs} = \begin{bmatrix} y_s \\ y_r \\ y_a \end{bmatrix} = \mathbf{C}_{cl}\left(\frac{\mathbf{B}_{clf}}{s\mathbf{I}-\mathbf{A}_{cl}}\cdot\mathbf{f}_u\right) + \begin{bmatrix}\mathbf{D}_{sf}\\ \mathbf{D}_{if}\end{bmatrix}\cdot\mathbf{f}_u. \tag{3.5}$$

4. Unbalanced response characteristic simulation

The ranges of the controller parameters ($K_p \in (0.27,\ 0.80)$, $K_d \in (3.0\cdot10^{-4},\ 11.0\cdot10^{-4})$) ensure rotor stable, which can be proved by the Routh-Hurwitz criterion [8]. According to the AMB structure, the coil current should not exceed 5 A to avoid saturating the magnetic field, which means the maximum bias current should less than 2.5 A.

A set of control parameters within the above range can be selected as: $K_p = 0.35$, $K_d = 6.0\cdot10^{-4}$, $i_0 = 1.4$. These parameters are consistent with those used in the simulation unless explicitly stated otherwise.

The steady-state unbalanced responses calculated by Eq. (3.4) are shown in Fig. 11. It shows that the vibration distributions at the upper and lower AMB are very close. The vibrations reach their maximum at 28 Hz, with displacements and currents peaking at 88/66 μm and 1.92/1.81 A, respectively.

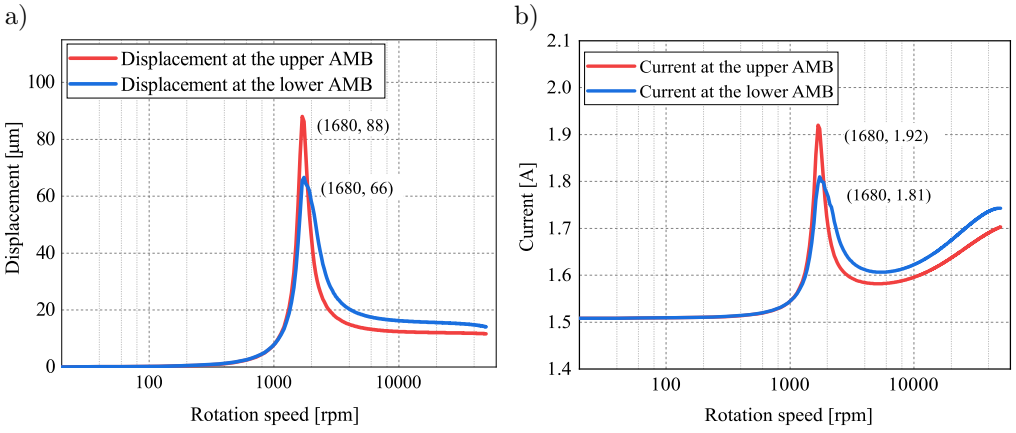

Fig. 11. Simulation of the unbalanced response for displacement (a) and current (b).

Within the rated speed range, the frequency at which the displacement reaches its maximum can be considered the rigid body critical speed. How these parameters affect the critical speed and the vibration peak will be discussed in the following section.

4.1. The effect on critical speed

Figure 12 illustrates the critical speeds varying as a function of K_p and K_d. Figure 12a shows that as K_p increases from 0.2 to 0.8, the rigid body's critical speed increases from approximately 20 Hz to around 53 Hz, and the rate of increase gradually slowing down. This indicates that adjusting K_p can potentially avoid critical speeds and reduce violent vibrations during run-up, leading to more stable operation. Furthermore, as K_p increases, a negative correlation between critical speed and K_d gradually becomes a positive correlation. However, overall, K_d has little impact on the critical speed for the same K_p.

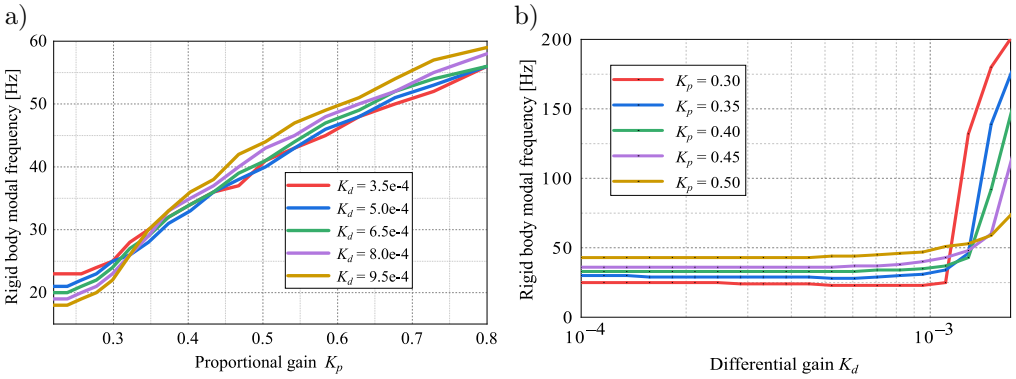

FIG. 12. Critical speeds as a function of proportional gain (a) and differential gain (b).

Figure 12b shows that with an increase in K_d from 0.0002 to 0.0011, the rigid body's critical speed remains steady at around 30 Hz. However, beyond 0.0011, the critical speed becomes extremely sensitive to K_d, indicating that within the proper range, K_d has little effect on the critical speed. However, when K_d is large, even slight variations can significantly change the critical speed.

4.2. The effect on unbalanced peaks

Figure 13 shows the variation in vibration peaks of the unbalanced response as a function of K_p. The results indicate that both the displacement and current peaks initially increase and then decrease with increasing K_p. During this process, their extreme values decrease with increasing K_d.

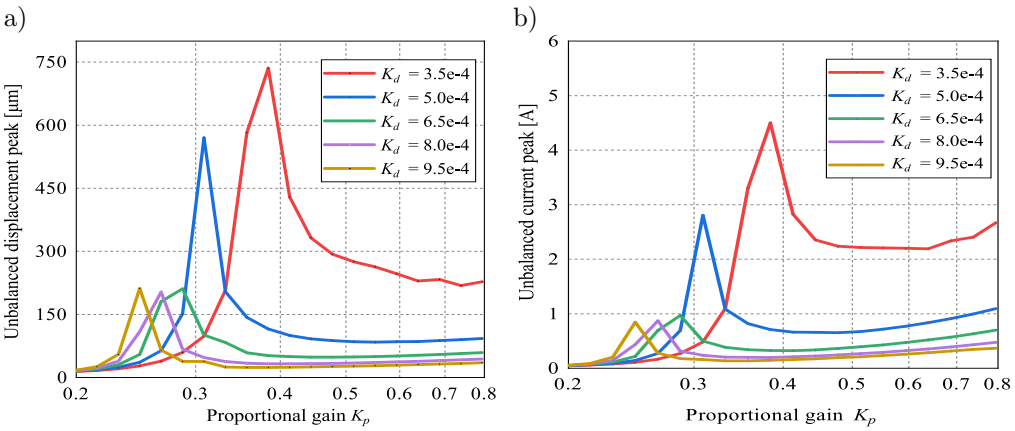

FIG. 13. Displacement peaks (a) and current peaks (b) of unbalanced response as a function of K_p.

The variation tendencies shown in Fig. 14 are similar to those in Fig. 13, where the values first increase and then decrease with increasing K_d. However, their extreme values increase with increasing K_p, implying that an increase in K_p aggravates the vibration when K_d is small.

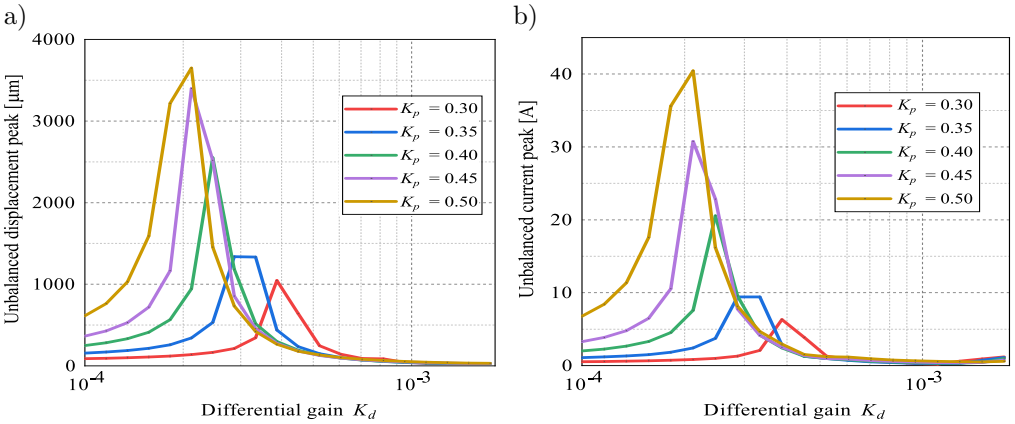

FIG. 14. Displacement peaks (a) and current peaks (b) of unbalanced response as a function of K_d.

Although some experimental results [23, 24] have shown that tuning the controller can simultaneously reduce both displacement and current response at the mode frequency, this paper further confirms this phenomenon through simulation results. It demonstrates that displacement and current are not in a compromise relationship at the rigid mode. They can be simultaneously suppressed by choosing an appropriate set of control parameters.

5. Experiment

5.1. Test rig for speed-up experiment

The compressor test rig mainly consists of a cold compressor prototype, an electronic control hardware system, and a monitoring system, as shown in Fig. 15. The rotor runs from a static state to 50 000 rpm at a rate of 500 rpm/s.

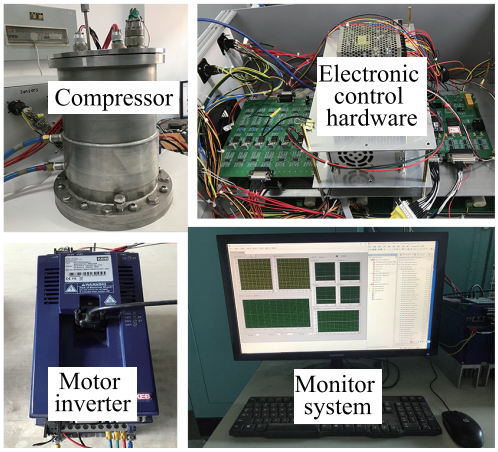

Fig. 15. Test rig for magnetic levitation compressor.

Based on the above simulation results, when $K_p \in (0.35,\ 0.50)$ and $K_d \in (4.5 \cdot 10^{-4}, 6.5 \cdot 10^{-4})$, the rotor can stably levitate and rotate relatively smoothly. Within these ranges, we select five sets of proportional gains and five sets of differential gains and record the rotor's vibration information during the run-up.

5.2. The effect of proportional gain

Figure 16 shows the displacement and current vibration information in the x-direction of the upper AMB when the differential gains is kept constant at $6.0 \cdot 10^{-4}$, and the proportional gains are 0.30, 0.35, 0.40, 045, 0.50, respectively. The results show that as the proportional gain increases, the rotor's rigid body critical speed increases from 25 Hz to 50 Hz. Both displacement vibration and current vibration simultaneously decrease at the resonance frequency as the proportional gain increases. However, the rotor controlled by a high proportional gain experiences strong vibrations when running at high speeds. This may be caused by the increase in resultant stiffness and reduced system damping as the speed increases.

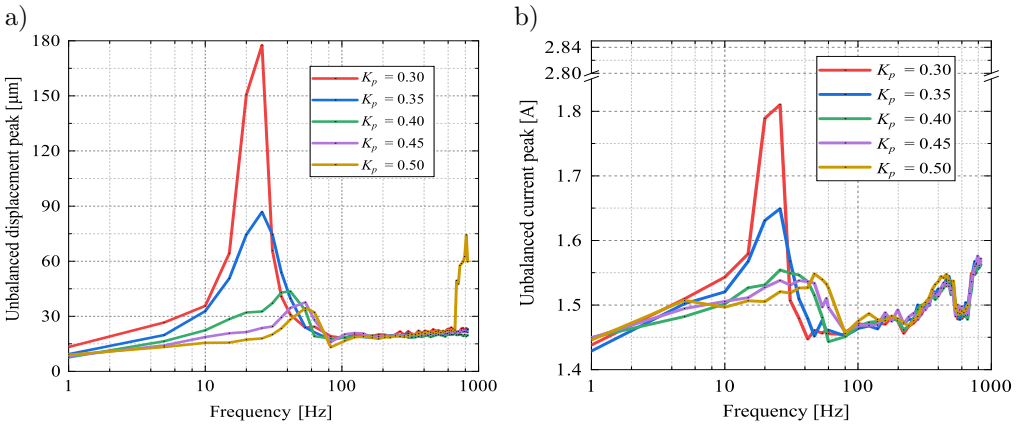

FIG. 16. The unbalanced displacement (a) and current response (b) in the experiment with different K_p.

5.3. The effect of differential gain

Figure 17 shows the displacement and current vibration information when the proportional gains are kept constant, and the differential gains are $4.5 \cdot 10^{-4}$, $5.0 \cdot 10^{-4}$, $6.0 \cdot 10^{-4}$, and $6.5 \cdot 10^{-4}$, respectively. The results indicate presents that the critical speed remains around 30 Hz, showing insensitivity to the differential gain. Both displacement and current vibration simultaneously decrease significantly with increasing differential gain at the rigid body frequency. Beyond the resonance frequency, the rotor runs stably and is almost unaffected by either the proportional gain or the differential gain.

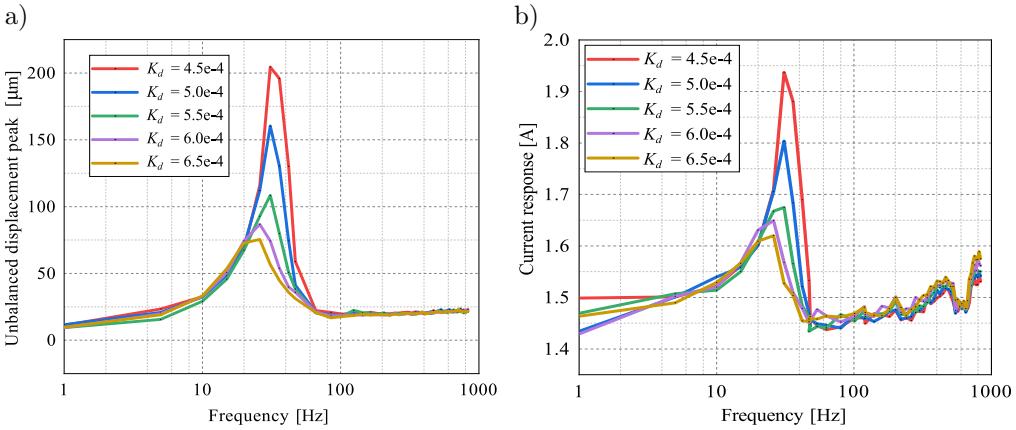

FIG. 17. The unbalanced displacement (a) and current response (b) in the experiment with different K_d.

6. Conclusion

This study utilized the state-space method and PID control strategy to successfully develop a closed-loop model for the magnetic levitation rotor system. This approach significantly improved the system's frequency response characteristics and control accuracy. Through simulations and experimental methods, we explored the intuitive relationship between control parameters and system response, highlighting the advantages of PID control in terms of system stability and ease of debugging. This research provides essential theoretical support and practical guidelines for the deployment and application of cold compressors in large superfluid helium cryogenic systems. Looking ahead, adaptive control strategies hold considerable promise for enhancing system responsiveness and efficiency, particularly well-suited for cold compressors operating in highly specialized environments. This study lays a solid foundation for future research into adaptive control solutions that could significantly improve performance under various operational conditions.

Funding

The authors grateful acknowledge the Initial Research Fund from Chuzhou University (No. 2023qd15).

Acknowledgments

The authors kindly thank the funder for their support.

Conflicts of interest

On behalf of all authors, the corresponding author states that there is no conflict of interest.

References

1. Kuendig A., Schoenfeld H., Voigt Th., Kurtcuoglu K., Yoshinaga S., Saji N., Shimba T., Honda T., Chapter 247: The cold-compressor systems for the LHC cryoplants at CERN, *Proceedings of the Twentieth International Cryogenic Engineering Conference (ICEC20)*, pp. 1043–1046, 2005, doi: 10.1016/B978-008044559-5/50250-7.

2. Schweitzer G., Maslen E.H. [Eds], *Magnetic Bearings: Theory, Design, and Application to Rotating Machinery*, Springer, Berlin, 2009.

3. Zhang S.Y., Pan W., Wei C.B., Wu J.H., Structure design and simulation research of active magnetic bearing for helium centrifugal cold compressor, *IOP Confer-*

ence Series: Materials Science and Engineering, **278**: 012162, 2017, doi: 10.1088/1757-899X/278/1/012162.

4. Huynh V.V., Tran M.H.Q., Integral sliding mode control approach for 3-pole active magnetic bearing system, *Applied Mechanics and Materials*, **829**: 128–132, 2016, doi: 10.4028/www.scientific.net/AMM.829.128.

5. Pesch A.H., Sawicki J.T., Active magnetic bearing online levitation recovery through μ-synthesis robust control, *Actuators*, **6**(1): 2, 2017, doi: 10.3390/act6010002.

6. Zhang S.Y., Wei C.B., Yang S.Q., Jia Q.M., Dong X.B., Wu J.H., Robust control of active magnetic bearing systems for helium centrifugal cold compressors, *IOP Conference Series: Materials Science and Engineering*, **502**: 012055, 2018, doi: 10.1088/1757-899X/502/1/012055.

7. Park C.H., Choi S.K., Ham S.Y., Design of magnetic bearings for turbo refrigerant compressors, *Mechanics & Industry*, **15**(4): 245–252, 2014, doi: 10.1051/meca/2014032.

8. Zhang S.Y., Chen Z.B., Lva X.L., Yan H.L., Wu J.H., Zhou Y.L., Dynamic characteristics analysis of magnetic levitation rotor considering unbalanced magnetic pull, *Applied Computational Electromagnetics Society Journal (ACES)*, **37**(10): 1096–1109, 2022, doi: 10.13052/2022.ACES.J.371010.

9. Wei C., Söffker D., Optimization strategy for PID-controller design of AMB rotor systems, *IEEE Transactions on Control Systems Technology*, **24**(3): 788–803, 2016, doi: 10.1109/TCST.2015.2476780.

10. Wang Z., Mao C., Zhu C., A design method of PID controller for active magnetic bearings-rigid rotor systems [in Chinese], *Proceedings of the Chinese Society of Electrical Engineering*, **38**(20): 6154–6163, 2018, doi: 10.13334/j.0258-8013.pcsee.171472.

11. Du G., Shi Z., Zuo H., Zhao L., Sun Z., Analysis of unbalanced response of rigid rotor supported by AMBs under coupling dynamic and control methods, *Applied Computational Electromagnetics Society Journal*, **34**(4): 512–519, 2019.

12. Wang D., Wang N., Chen K., Ye C., Dynamic characteristics of magnetic suspended dual-rotor System by RICCATI transfer matrix method, *Shock and Vibration*, **2019**(1): 9843732, 2019, doi: 10.1155/2019/9843732.

13. Tang E., Fang J., Han B., Active vibration control of the flexible rotor in high energy density magnetically suspended motor with mode separation method, *ASME Journal of Engineering for Gas Turbines and Power*, **137**(8): 082503, 2015, doi: 10.1115/1.4029372.

14. Wang D., Wang N., Chen K., Unbalance response of a magnetic suspended dual-rotor system, *Proceedings of the Institution of Mechanical Engineers, Part G: Journal of Aerospace Engineering*, **233**(15): 5758–5772, 2019, doi: 10.1177/0954410019858011.

15. Gao H., Meng X., Qian K., The impact analysis of beating vibration for active magnetic bearing, *IEEE Access*, **7**: 134104–134112, 2019, doi: 10.1109/ACCESS.2019.2932723.

16. Liu Y., Ming S., Zhao S., Han J., Ma Y., Research on automatic balance control of active magnetic bearing-rigid rotor system, *Shock and Vibration*, **2019**(1): 3094215, 2019, doi: 10.1155/2019/3094215.

17. Lei S., Palazzolo A., Control of flexible rotor systems with active magnetic bearings, *Journal of Sound and Vibration*, **314**(1–2): 19–38, 2008, doi: 10.1016/j.jsv.2007.12.028.

18. Numanoy N., Srisertpol J., Vibration reduction of an overhung rotor supported by an active magnetic bearing using a decoupling control system, *Machines*, **7**(4): 73, 2019, doi: 10.3390/machines7040073.

19. Skogestad S., Postlethwaite I., *Multivariable Feedback: Control Analysis and Design*, John Wiley & Son, Chichester, 2001.

20. Becker F.B., Sehr M.A., Rinderknecht S., Vibration isolation for parameter-varying rotor systems using piezoelectric actuators and gain-scheduled control, *Journal of Intelligent Material Systems and Structures*, **28**(16): 2286–2297, 2017, doi: 10.1177/1045389X17689933.

21. Gu H., Zhao L., Shi L., Diao X., Controller design for a flexible rotor supported by active magnetic bearing passing the critical rotational speed, *Journal of Tsinghua University*, **45**(6): 821–823, 2005.

22. Maslen E.H., Knospe C.R., Zhu L., An enhanced dynamic model for the actuator/amplifier pair in AMB systems, *Proceedings of the 10th International Symposium on Magnetic Bearings*, Martigny, 2006.

23. Wang Y., Fang J., Zheng S., Optimal phase compensation control and experimental study of flexible rotor supported by magnetic bearing, [in:] *Proceedings of the 2012 8th IEEE International Symposium on Instrumentation & Control Technology*, London, 2012, pp. 314–319, doi: 10.1109/ISICT.2012.6291635.

24. Fang J., Tang E., Zheng S., Optimum damping control of the flexible rotor in high energy density magnetically suspended motor, *ASME Journal of Engineering for Gas Turbines and Power*, **137**(8): 082505, 2015, doi: 10.1115/1.4029393.

Received January 2, 2024; accepted version August 2, 2024.
Online first September 17, 2024.